energies

MDPI

Article

Thermal Performance and Numerical Simulation of the 1-Pyrene Carboxylic-Acid Functionalized Graphene Nanofluids in a Sintered Wick Heat Pipe

Alireza Esmaeilzadeh [1], Mahyar Silakhori [2,*], Nik Nazri Nik Ghazali [3,*], Hendrik Simon Cornelis Metselaar [1], Azuddin Bin Mamat [3], Mohammad Sajad Naghavi Sanjani [1] and Soudeh Iranmanesh [4]

[1] Centre of Advanced Materials, Department of Mechanical Engineering, Faculty of Engineering, University of Malaya, Kuala Lumpur 50603, Malaysia; aesmaeilzadeh2@gmail.com (A.E.); h.metselaar@um.edu.my (H.S.C.M.); sajad.naghavi@um.edu.my (M.S.N.S.)
[2] School of Mechanical Engineering, The University of Adelaide, Adelaide, SA 5005, Australia
[3] Department of Mechanical Engineering, Faculty of Engineering, University of Malaya, Kuala Lumpur 50603, Malaysia; azuddin@um.edu.my
[4] Department of Materials Science and Engineering, Faculty of Engineering, Arak University, Arak 3848170001, Iran; soudeh.irmanesh@gmail.com
* Correspondence: mahyar.silakhori@adelaide.edu.au (M.S.); nik_nazri@um.edu.my (N.N.N.G.)

Received: 16 November 2020; Accepted: 8 December 2020; Published: 11 December 2020

Abstract: Experimental and numerical modeling of a heat pipe included with a phase change heat transfer was developed to assess the effects of three parameters of nanofluid, heat pipe inclination angles, and input heating power. Distilled water (DW) and 1-pyrene carboxylic-acid (PCA)-functionalized graphene nanofluid (with concentrations of 0.06 wt%) were used as working fluids in the heat pipe. A computational fluid dynamic (CFD) model was developed for evaluation of the heat transfer and two-phase flow through the steady-state process of the heat pipe. It was found that inclination significantly affects the heat transfer of the heat pipe. Maximum increment of thermal performance in the heat pipe reached 49.4% by using 0.06 wt% of PCA-functionalized graphene as working fluids. The result associated with this comparison indicates that the highest deviation is less than 6%, consequently confirming that the CFD model was successful in reproducing the heat and mass transfer processes in the DW and nanofluids charged heat pipe. The results of CFD simulation have good agreement between predicted temperature profiles and experimental data.

Keywords: computational fluid dynamics; multiphase flow; nanofluid; graphene; heat pipe; sintered wick heat pipe

1. Introduction

Heat transfer and energy supply contribute vastly to different domains such as electronic tools and energy production. The role of heat pipes performance is very crucial in numerous industries such as heating, ventilation, and air conditioning (HVAC) and solar thermal system [1–4]. One of the methods to excel the function of heat pipe is to use highly efficient fluid and proper design of the internal wall of heat pipe. Although there are several investigations on the performance of heat pipe with nanofluids, there is a need to assess the effect of new material on the performance of heat pipe.

A heat pipe is a device with a high operative heat transfer rate in evaporating and condensing a fluid that transfers the heat in two phases. A two-phase closed thermosyphon or a wickless heat pipe uses the gravitational forces to transfer the working fluid to the evaporator. The main difference with wicked heat pipe is in the condenser section, which capillary forces cause to the return of the

working fluid [5,6]. Due to flexibility, simplicity of structure, good compactness, excellent reversibility, and high efficiency of heat pipes [7,8], these devices have been applied for the recovery of waste energy in a variety of applications including HVAC [9], heat source [10,11], ground source heat pumps [12], ventilation, electronics thermal management [13], and water heating systems [14].

Extensive research works have been published to examine the efficiency of the nanofluids in heat pipes [15–18]. Heat transfer coefficient, thermal performance, and axial heat pipe's wall temperature are among the standard functional specifications that the tests were conducted [19]. Kim et al. [20] studied effect of using Graphene and Acetone in the heat delivery efficiency of a thermosiphon. The authors claimed that a 70.3% thermal resistance was observed compared to acetone under the same experimental procedure. Mehrali et al. [21] claimed the heat transfer coefficient was raised by 61.25% in the evaporator section when using 1 vol% diamond and distilled water (DW) nanofluid was evaluated. Goodarzi et al. [22] examined the function of Fe_2O_3-kerosene nanofluid in the copper oscillating heat pipe and reported a 16% improvement in thermal delivery of the heat pipe as compared with kerosene. Ghanbarpour et al. [23] claimed an 11% increase in the thermal conductivity by using aqueous Ag nanofluid as a working fluid. Naphon et al. [24] compared the thermal efficiency of TiO_2-alcohol nanofluid and DW and alcohol as a functioning fluid. They found that the thermal performance of the heat tube increased to 80% with the experimental condition of 45° inclined angle, heat flux of 7.27 kW/m^2, 66% filling ratio, and 0.1 vol% nanofluid concentration. To enhance the thermal efficiency of heat pipes, the selection of proper functioning fluid is crucial. It is important to choose a proper functioning fluid as the working fluid in the heat pipe as a closed-loop heat exchanger [25]. Homogeneous suspensions of nanoparticles in oil or distilled water form nanofluids are an effective parameter in heat exchanging between heat input and output [26].

Due to the flexibility, universality, efficiency, and accuracy of the computational simulation, numerous engineers use this way for explaining complex stream problems in many applications. Legierski et al. [27] analyzed—numerically and experimentally—thermal conductivity of a heat pipe in a transient state during in start-up and temperature increment. Zhang et al. [28] studied a disk-shaped flat two-phase thermosiphon used in electronics cooling and simulated it with a two-dimensional CFD model. Joudi and Al-Tabbakh [29] simulated a two-phase thermosiphon in a solar domestic hot water system with the R-11 as a working fluid. Then, they validated their simulation result with the results of those obtained with single-phase systems. Annamalai and Ramalingam [30] investigated an experimental and simulation analysis of a wicked heat pipe using ANSYS CFX. They validated their results such as vapor temperature and surface temperature along the evaporator and condenser walls with the experimental results. Schepper et al. [31] simulated the process of the evaporation with a hydrocarbon feedstock in a heat exchanger with using of volume of fluid (VOF) and user-defined function (UDF) techniques to simulate flow boiling including the phase change process.

The working fluid has significant effect on the performance of the heat pipe [32]. The majority of the metal oxide and metal nanoparticles show the difficulty of long-term stability [33]. Lack of potential for performing covalent functionalization causes increasing this problem. Therefore, the solution could be by presenting a carbon-based nanoparticle with the capability of covalent functionalization to solve the problem of stability. Attractive properties of graphene nanoplatelets (GNP) including fully nano-sized dimensions, high specific surface area [34], great stability in aqueous media [35], and promising thermophysical properties, makes it an excellent candidate to solve all the mentioned problems in comparison with the previous nanofluids. 1-pyrene carboxylic-acid (PCA) functionalization of graphene significantly increases the colloidal stability of water-based nanofluid and enhanced wettability of the electrolyte [36]. The carboxylic acid group (-COOH) that facilitates the GNP stability in water functionalizes the sidewalls via a nondestructive π-π stacking mechanism (aromatic interaction) [37].

In this paper, a CFD modeling for the operation of a sinter wick heat pipe has been used to study in detail the phenomena of heat transfer and two-phase flow. The assortment of working fluid in the heat pipe is significant to improve the thermal performance of the device. To examine the

effect of PCA-functionalized graphene nanofluid on the heat pipe performance, in the current study, we functionalized the GNP with 1- Pyrene Carboxylic-Acid. To the best of our knowledge, there has been no research on sintered wick heat pipes filled with PCA-functionalized graphene nanofluids.

2. Defining the Configuration and Nanofluid

The current investigation utilizes the thermal performance study of a sintered heat pipe by two-phase CFD modeling, and CFD simulation is validated with the experimental model.

2.1. Experimental Procedure

With the purpose of assessment of the thermal efficacy of a heat pipe, a standard test system consists of the experimental sector, heating section, and cooling section, a movable table with adjustable angle, data logger, and a computer unit were used, as illustrated in Figure 1.

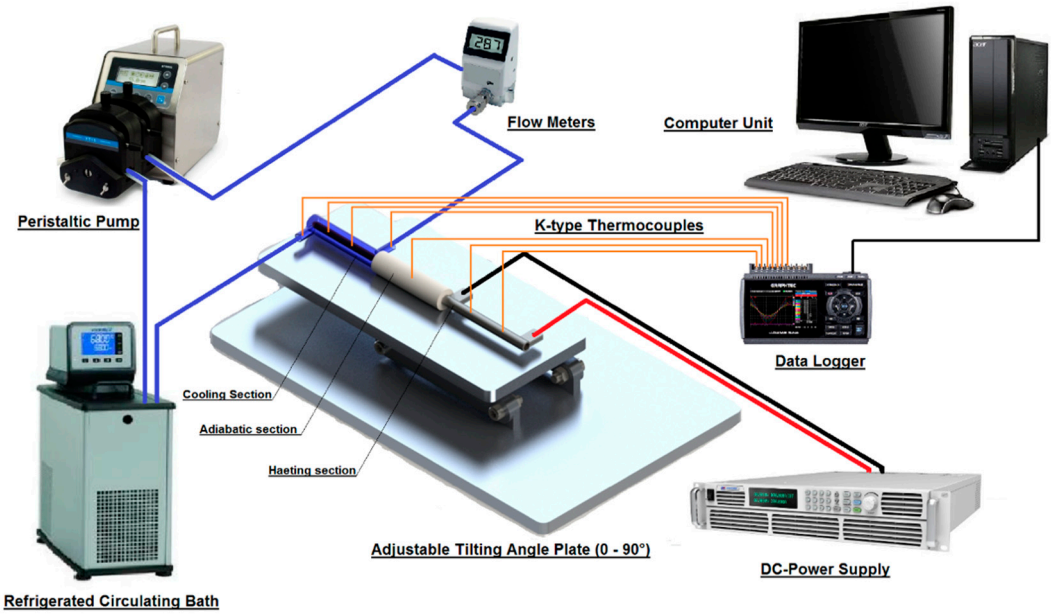

Figure 1. Schematic view of the experimental test rig.

To examine the condenser sector's input and output temperatures, 2 K-type thermocouples (Omega) were employed. The heat which was associated with a DC power supply (KEYSIGHT Technologies) is used in the evaporator section. The test sector is covered with numerous sheets of ceramic fiber to diminish the heat loss from the adiabatic, condenser, and evaporator sections. Figure 2 illustrated the schematic of the heat pipe in the experiment. Five self-adhering K-type thermocouples have been positioned at the wall surfaces of the heat tubes which consist of two thermocouples for the condenser, evaporator, and one for adiabatic sections, with distances of T1 = 50, T2 = 100, T3 = 150, T4 = 200, T5 = 250 mm from the start point of the evaporator section.

The wall temperatures of the heat pipe were measured with the aid of thermocouples, as shown in Figure 2 Thermocouple calibration was conducted before the experiments. To record and monitor the thermocouple temperature constantly, thermocouples were linked with the Graphtec data logger (midi logger GL220).

The test segment of the copper heat pipe is composed of a copper sintered wick tube with an external diameter of 10 mm, a length of 300 mm, a wall thickness of 0.5 mm, and a sintered wick thickness of 0.2 as shown in Figure 3. The copper pipe is supplied by Shenzhen Maoye Electronics Co. (Shenzhen, China).

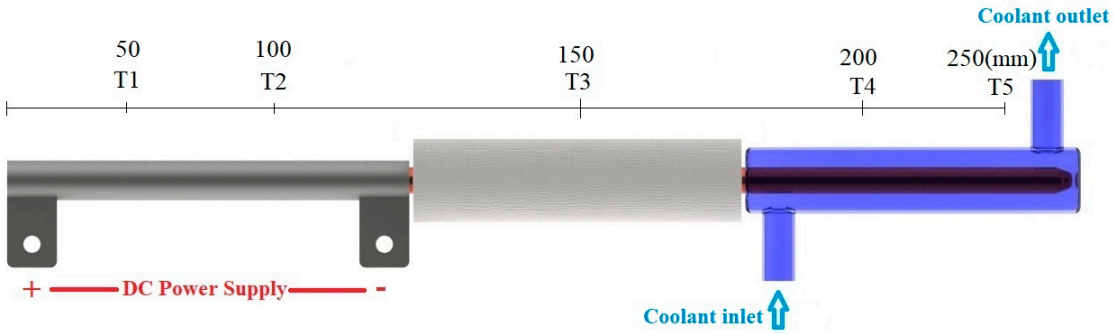

Figure 2. The schematic of the heat pipe in the experiment rig with the position of thermocouples.

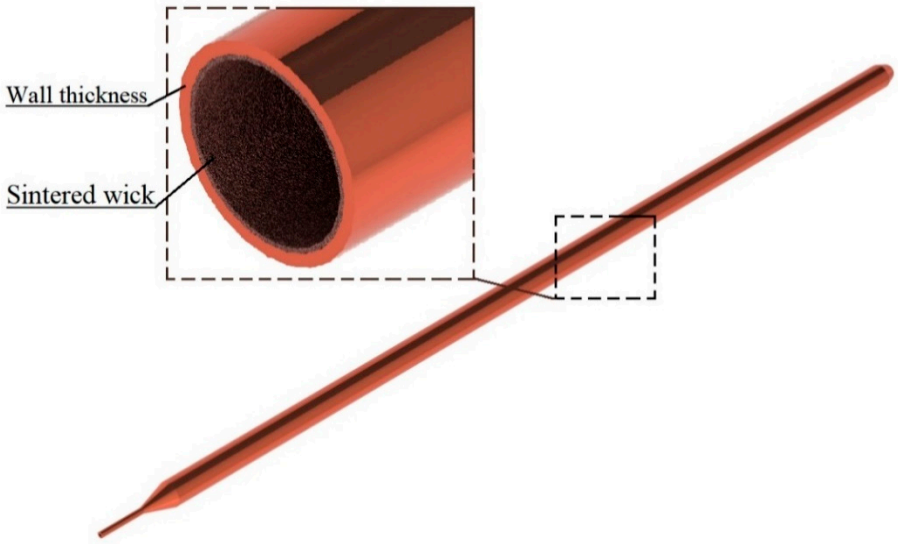

Figure 3. Model geometry of heat pipe.

2.1.1. Nanofluid Preparation and Stability

1-pyrene carboxylic acid (PCA), graphene nanoplatelets (GNP), ethanol, and distilled water (DW) have been utilized for the preparation of PCA-functionalized graphene nanofluids. PCA-functionalized graphene dispersions were prepared by sonicating a mixture of graphite powder (Aldrich, particle size <45 μm) and 1-pyrene carboxylic acid (Aldrich, 98%) in 50 mL methanol for 45 min with a Branson® 5510 bath sonicator. To this solution, 200 mL of distilled water was added (stage 1 of the process, see Figure 4A,B), and sonication was continued for a day. The dispersion was then allowed to settle overnight (stage 2, Figure 4A,B). The clear supernatant liquid was poured away, and distilled water was added. The solution was then sonicated for an additional two hours, resulting in a stable purplish-grey dispersion that does not show any significant precipitation at stage 3 when left on a lab benchtop for weeks.

One of the most important practical issues requiring special attention is the long-term stability of nanofluid. The aggregation of nanoparticles leads to non-homogeneity nanofluids due to strong Van der Waal's interaction. Therefore, some physical and chemical techniques such as applying strong force on the cluster of the suspend particle or using surfactant have been applied to get stable nanofluids. The stable homogeneous PCA-functionalized graphene nanofluids were prepared.

The morphology and microstructure of graphene nanoplatelets were observed using a scanning electron microscope (SEM) from LEO 1530 FE-SEM (Carl Zeiss, Munich, Germany), as shown in Figure 5. The PCA-functionalized graphene porous and uniform structures can be seen.

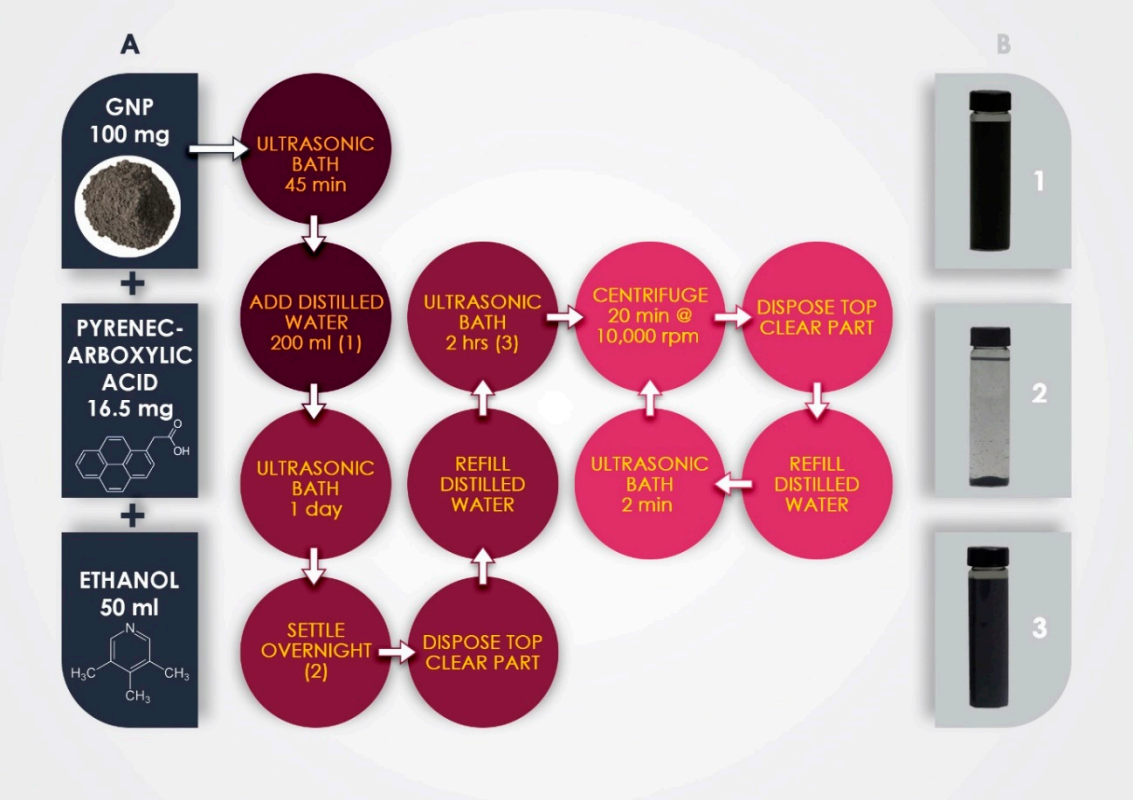

Figure 4. (**A**) Process Preparation of the aqueous 1-pyrene carboxylic-acid (PCA)-functionalized graphene nanofluids (**B**) Three stages of Preparation.

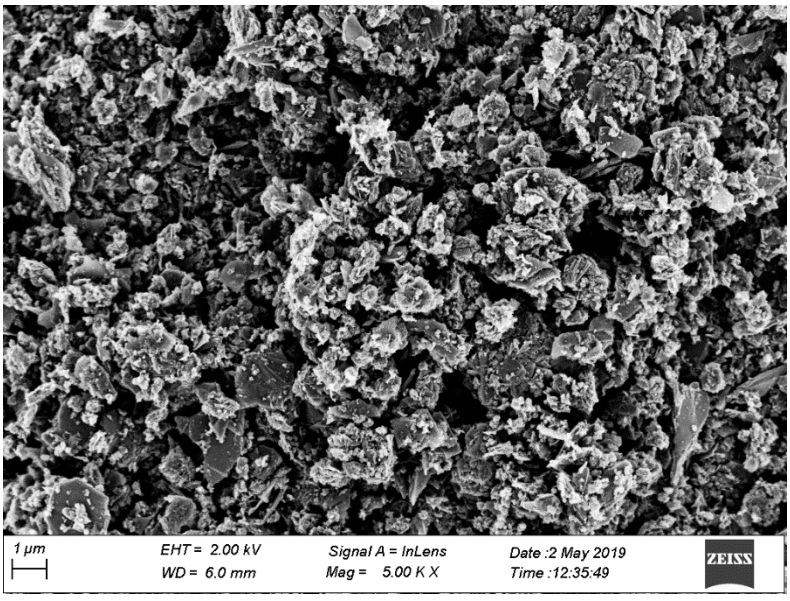

Figure 5. The SEM image of PCA-functionalized graphene.

2.1.2. Data Processing

PCA-functionalized graphene nanofluids were used due to investigating the thermal performance of the sintered wick heat pipe. To examine the thermal efficiency and heat transfer coefficient of the heated tube, an aqueous PCA-functionalized graphene nanofluid with 0.06 wt% was utilized. In this study, we only choose 0.06 wt% concentrations of nanofluid as a working fluid. An equal

quantity of working fluid (40% of heat pipe volume) will be loaded in each heat pipe and subsequently discharged to achieve vacuum pressure with the aid of the vacuum pump. The circulating of the cold water in the condenser section, and it is asserted under the following experimental conditions: 20 °C input temperature with a 400 mL/min flow rate. A variable angle holder table was utilized to modify the heat pipe inclination angle from 0° to 90°. Similarly, the DC power supply has been used to set heat power input for the evaporator section at 40, 60, 80,100, and 120 watts. A data logger was used to record the steady-state temperature data at a time interval of 1 s for 200 s (maintaining almost 60 min duration between each heat input augmentation). For data reduction and analysis, steady-state temperature data are also saved on the computer.

In addition, the reduction in the pressure of vapor and lower temperature gradient in the vapor region results in the temperature of the vapor through the evaporator and adiabatic segments. The inner wall surface temperature of the condenser section is lower than the external one, whereas the temperature of working fluid in the evaporator section remain lower than the outer surface temperature. This implies that to be able to calculate the heat transfer coefficients, the internal wall surface temperatures of the condenser and evaporator should be considered. The external surface temperature evaluation could be implemented with reasonable precision in assessing the thermal efficiency and thermal resistance of the heat pipe due to the lower radial thermal resistance of the copper heat tube wall and the copper sintered wick (~10 to 3 °C W). The temperature increases between the condenser and the evaporator part of the heat tube demonstrated the total thermal resistance of the heat pipe. The temperatures of evaporator [8], adiabatic section (T_{vap}) and condenser section (T_c) correspondingly are considered as follows: $T_e = (T_1 + T_2)/2$, $T_{vap} = T_3$, and $T_c = (T_4 + T_5)/2$.

The heat transfer coefficient of the evaporator was defined as

$$h_e = \frac{\dot{Q}}{A_e \Delta T} \tag{1}$$

$$\Delta T = T_e - T_{vap} \tag{2}$$

$$\dot{Q} = V \times I \tag{3}$$

where ΔT is the difference of heat among the surface of the heated tube and the vapor temperature, and T_{vap} is the temperature of saturated steam, which could be obtained from the surface of the adiabatic part. Moreover, $\dot{Q}$ represents the heat input power which regulate by Voltage (V) and amperage (I).

The heat pipe's thermal efficiency is the ratio of the heat removed in the condenser section to the heat supplied in the evaporator section. It is given by

$$\eta = \frac{\dot{Q}_c}{\dot{Q}} = \frac{\dot{m} C_{p,w} \Delta T_w}{V \times I} \tag{4}$$

Here, Q_c represents the heat transfer rate which the cooling water is removed from the condenser. $\dot{m}$, $C_{p,w}$, and ΔT_w be present the mass flow rate, specific heat, and temperature growth of the cooling water, respectively. The suspicion of the estimated parameters is assessed depending on the precision of the tools. All the test tools are recalibrated, and the vulnerability outcomes are shown in Table 1, with the most extreme value recorded for each situation.

Table 1. The rate of uncertainty ranges for selected parameters.

Parameters	Error (%)
Temperature	0.2
Length of the heated section	2.3
The diameter of the heat pipe	2
Heat input	3.3
Heat flux	3.2
Thermal resistance	4.1
Heat transfer coefficient	3.5

2.2. Numerical Analysis

In this study, the ANSYS FLUENT 19.0 software was used and for the modeling of a heat pipe, the volume of fluid (VOF) method has been applied. The aim of this paper is the CFD analysis of the thermal performance of nanofluids in a heat pipe. Hence, a turbulent multiphase flow system without chemical reaction has been considered in this thermal scheme. The volume of fluid (VOF) model was used to model the evaporation and condensation of fluid inside the heat pipe. A single set of momentum equations will be solved and the volume fraction of each fluid throughout the domain will be tracked with the VOF model by considering two or more immiscible fluids, and the volume fraction of each fluid in all computational cell is tracked throughout the domain [38].

2.2.1. Physical Model Description and Boundary Conditions

Figure 6 shows the 2D geometrical configuration of the model for CFD simulation. The proportions of this geometry have been chosen as same as the dimensions of the experimental setup used. The length of 100 mm has been taken for evaporator, adiabatic, and condenser sections of the heat pipe. The wall and wick structure are copper material. DW and PCA-functionalized graphene nanofluid are considered as working fluid in this paper.

In this study, thermal conductivity was measured by the hot-wire transient method. KD2 Pro thermal conductivity analyzer (Decagon Devices, Inc., Pullman, Washington, USA) with 5% error rate has been used to measure the thermal conductivity of the PCA-functionalized graphene nanofluids. Further, one layer of the sintered wick by a thickness, porosity, and the thermal conductivity of 0.2 mm, 0.43, and 1.17 W/m-K, correspondingly are measured. An Anton Paar rheometer (Physica MCR 301, Anton Paar GmbH, Graz, Austria) has been used to measure the viscosity of nanofluid with a 1% error rate. Before using the nanofluids, it was calibrated with the distilled water. Table 2 shows the thermophysical properties of the working fluid, wick structure, and wall. Two sides of the heat pipe wall considered to be wick.

The cooling system in the condenser section and the heating system in the evaporator section are used as boundary conditions. Except evaporator and condenser sections, the other surfaces considered to have adiabatic boundary conditions as shown in Figure 7. The gravity, in heat pipe technology, has one positive side once certify the rotation of the working fluid in the gravity heat pipe (thermosiphon) and one negative side, when turn opposite the capillary action in the wick heat pipe [39]. In this study, we also emphasized the influence of working position on heat transfer capability of the wick heat pipe. As illustrated in Figure 7, the several working positions range from vertical to horizontal with the sequence of the inclination angle about 30° was realized.

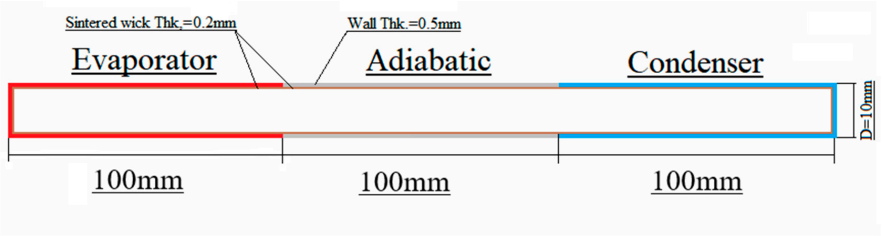

(**a**)

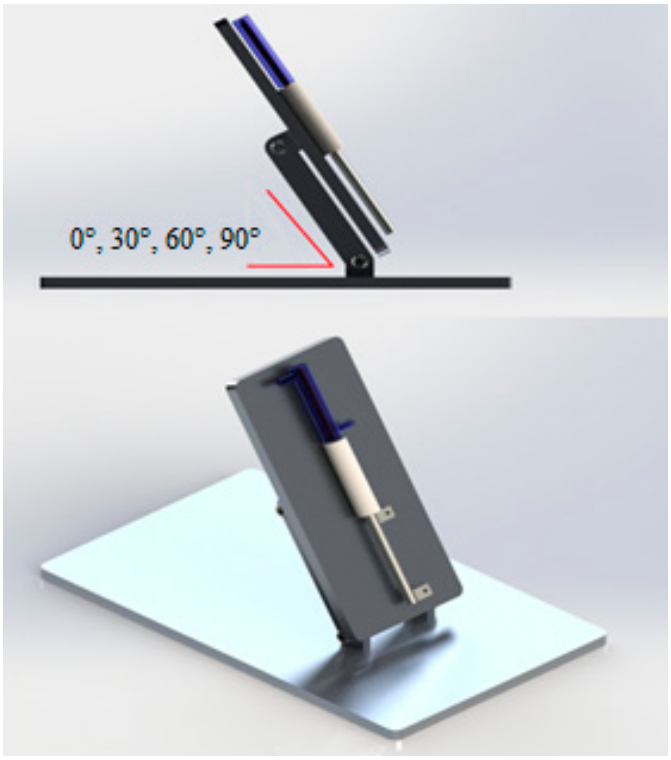

(**b**)

Figure 6. (**a**) Geometrical configuration of the heat pipe, (**b**) and schematic of the mounting platform with different tilt angles.

Table 2. The working fluid and heat pipe material properties.

Copper wall/wick	Thermal conductivity	387.6 W/m K
	Specific heat	381 J/kg K
	Density	8978 kg/m^3
	Thermal conductivity of the wick	40 W/m K
Water	Thermal conductivity	0.6 W/m K
	Specific heat	4182 J/kg K
	Density	1000 kg/m^3
	Viscosity	1.05 mPas
Water vapor	Thermal conductivity	0.026 W/m K
	Specific heat	2014 J/kg K
	Density	0.01 kg/m^3
	Viscosity	0.00849 mPas
Water/vapor	Latent heat of vaporization	2446.36 kJ/kg
PCA-functionalized graphene nanofluid with 0.06 wt%	Viscosity	1.23 mPas
	Density	1025 kg/m^3
	Specific heat	4210 J/kg K
	Thermal conductivity	0.79 W/m K

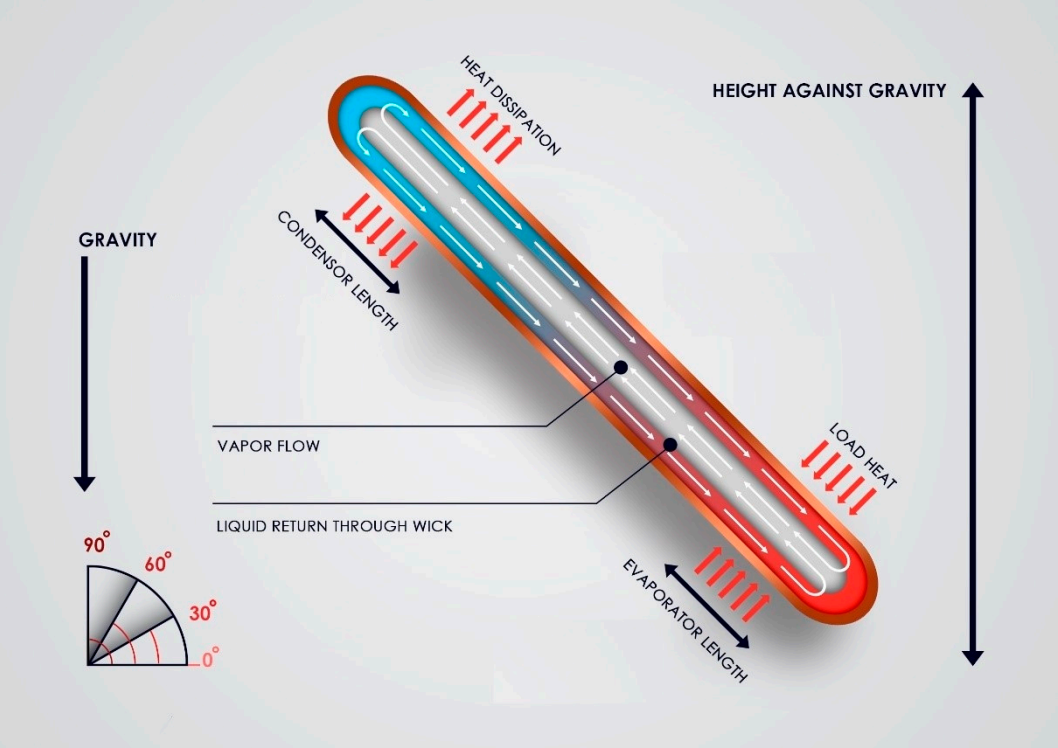

Figure 7. Schematic of the boundary conditions and heat transfer processes of the heat pipe.

At the walls of the heat pipe, a no-slip boundary condition was used. The no-slip condition of viscous fluids was performed in fluid dynamics that state the fluid will have zero velocity relative to the boundary of a solid boundary. The constant heat flux applied to the walls of evaporator and condenser sections and the zero-heat flux boundary condition was applied for adiabatic walls as a default condition for all walls. (Figure 7).

It has been implicit that the condenser is chilled by water, as claimed by the experimental procedure. Hence, a convection heat transfer coefficient was demarcated as a boundary condition on the condenser's wall. The conforming heat transfer coefficients have been considered with the formula [40].

$$h_c = \frac{Q_c}{2\pi r L_c (T_{c.av} - T_\infty)} \tag{5}$$

where Q_c is the rate of heat transfer from the condenser, $T_{c.av}$ is the condenser average temperature, L_c is the condenser height, r is the pipe radius, T_∞ is the average temperature of the condenser cooling water, and h_c is the condenser heat transfer coefficient. Figure 7 shows the boundary conditions applied to the computational model.

2.2.2. Assumptions and Governing Equations

The following assumptions have been used:
Body forces are negligible.

- Vapor and liquid flows are turbulent and incompressible.
- The volume is an average of density of the liquid in the wick is reformed to preserve liquid mass and to contain the variations in vapor and liquid mass correctly through the transient operational conditions [41].
- The vapor is saturated at t = 0 (time).
- Thermophysical properties are supposed constant excluding the vapor density, which is calculated from the working pressure.

Surface tracking technique of VOF model applied to the fixed Eulerian mesh. This method consists of two volume fractions of α_l and α_v which represent the location of liquid and vaper and interface in computational cells. When $\alpha_v = 0$ the liquid phase occurs, and vaper phase happen only where $\alpha_v = 1$. Generally liquid–vapor interface detects in the cell wherever $0 < \alpha_v < 1$. The volume fractions of all phases sum up in each control volume.

$$\alpha_v + \alpha_l = 1 \tag{6}$$

The continuity equation of volume fraction for both phases can provide the interface tracking between the phases. The following equation indicate the phase q.

$$\frac{1}{\rho_q}\left[\frac{\partial}{\partial t}\left(\alpha_q \rho_q\right) + \nabla.\left(\alpha_q \rho_q \vec{v}_q\right) = S_{\alpha_q} + \sum_{p=1}^{n}\left(\dot{m}_{pq} - \dot{m}_{qp}\right)\right] \tag{7}$$

The mass transfer from phase q to phase p shows by $\dot{m}_{qp}$ and $\dot{m}_{pq}$ present the mass transfer from p to q. The void fraction represents by α and ρ signify the density as well. The basis term on right side of this equation is S_{α_q} which equal to zero.

The equation of momentum is as follows:

$$\frac{\partial}{\partial t}\left(\rho \vec{v}\right) + \nabla.\left(\rho \vec{v}\vec{v}\right) = -\nabla \mathrm{p} + \nabla.\left[\mu\left(\nabla_{\vec{v}} + \nabla_{\vec{v}^T}\right)\right] + \rho \vec{g} \tag{8}$$

The flow inside the heat pipe considered to be turbulent, therefore the turbulent K-ε model equations are as follows:

$$p' = \mathrm{p} + \frac{2}{3}\rho k + \frac{2}{3}\mu_{eff}\frac{\partial U_k}{\partial x_k} \tag{9}$$

$$\mu_{eff} = \mu_t + \mu \tag{10}$$

p' is defined as the corrected pressure, and μ_t is the turbulence viscosity.

$$\frac{\partial}{\partial xj}(\rho k U_i) = \frac{\partial}{\partial xj}[(\mu + \frac{\mu_t}{\sigma_k})\frac{\partial K}{\partial xj}] + G_k + Y_m - \rho\varepsilon \tag{11}$$

$$\frac{\partial}{\partial xj}(\rho \varepsilon U_i) = \frac{\partial}{\partial xj}[(\mu + \frac{\mu_t}{\sigma_\varepsilon})\frac{\partial \varepsilon}{\partial xj}] + c_{1\varepsilon}\frac{\varepsilon}{K}G_k - c_{2\varepsilon}\rho\frac{\varepsilon^2}{K} \tag{12}$$

G_k Refers to the generation of turbulent kinetic energy due to the average velocity gradient, and the expression Y_m represents the contribution of velocity fluctuations in a turbulent flow. Further, $c_{1\varepsilon}$ = 1.44 and $c_{2\varepsilon}$ = 1.92 has been chosen constant coefficients according to the Fluent Program Guide [42].

Furthermore, σ_k and σ_ε represent prantel numbers of turbulences for k-ε that are considered as follows:

$$\sigma_k = 1,\ \sigma_\varepsilon = 1.3$$

The viscosity of the turbulence μ_t is similarly considered according to k-ε values as follows:

$$\mu_t = \rho C_\mu \frac{k^2}{\varepsilon} \tag{13}$$

Constant C_μ also, we considered as 0.09.

Energy equation of the VOF model is as follows:

$$\frac{\partial}{\partial t}(\rho E) + \nabla.\left(\vec{v}(\rho E + P)\right) = \nabla.\left(k_{eff}\,\nabla \mathrm{T}\right) + S_h \tag{14}$$

The averaged variables of energy E and temperature T are treats the VOF model.

$$\mathrm{E} = \frac{\sum_{q=1}^{n} \alpha_q \rho_q E_q}{\sum_{q=1}^{n} \alpha_q \rho_q} \tag{15}$$

For each phase the E_q is created by specific heat of that phase and the temperature. The properties of density ρ and effective thermal conductivity k_{eff} are based on Table 2. S_h represent the source of radiation, along with any other heat sources.

The next term of Equation (16) is ignored for the solid regions. k_{eff} is the effective thermal conductivity of the section of notice such as tube wall, liquid wick combination, and the vapor. The hermal conductivity of the wall is according to Table 2. k_{eff} of the liquid–wick mixture is calculated as follows:

$$k_{eff} = k_l \left[\frac{(k_l + k_w) - (1-\varepsilon)(k_l - k_w)}{(k_l + k_w) + (1-\varepsilon)(k_l - k_w)} \right] \tag{16}$$

k_l is the thermal conductivity of the working fluid and k_w is the thermal conductivity of the wick structure in Equation (17). The porosity of the wick through by the nanofluid is calculated with the following equation:

$$\varepsilon = 1 - \frac{1.05\pi N d_\omega}{4} \tag{17}$$

When nanofluid is replaced as a replacement for DW, the effective thermal conductivity of the liquid–wick mixture variations from 1.11 to 1.69 W/m-K. Following equation shows the permeability of the wick structure:

$$K = \frac{d_\omega^2 \varepsilon^2}{122(1-\varepsilon)^2} \tag{18}$$

Depositions of the nanoparticles increase the wire diameter of the wick that cause changes of the k_{eff} that is initiate to be 1.75 W/m-K.

The governing equations were numerically explained by the finite volume method in Ansys Fluent software.

2.2.3. Mesh Independency

Numerous meshes are assessed to remove the mesh sensitivity and reduction of the calculation's requirement. Table 3 shows the evaluation of the dependence of results on the mesh. The grid study of the results is checked by growing the mesh numbers. These results show the maximum and average temperature on the evaporator and condenser of the heat pipe that is occupied with DW and working at θ = 90° and 120 W heat input. The results show that 2.2 × 105 cells are appropriate for obtaining satisfactory results. The grids were concentrated near the walls due to a very thin layer of liquid near there. The initial row, growth factor, and a number of rows of the shaped boundary layer are 0.03, 1.3, and 8, correspondingly.

Table 3. The grid study results.

Number of Elements	Average Temperature on Evaporator Sections (°C)	Maximum Temperature on Evaporator Sections (°C)	Average Temperature on Condenser Sections (°C)	Maximum Temperature on Condenser Sections (°C)
110,991	77.1	79.3	44.8	45.9
155,910	77.9	79.7	45.7	47.1
210,510	78.9	80.3	46.8	47.8
225,229	79.7	80.1	47.2	47.6
290,519	79.8	80.1	47.3	47.8

2.2.4. Uncertainty Analysis

With reading the temperature that was quantified using K-type thermocouples with (0.05% rdg + 0.3 °C) and 0.5% rdg for the uncertainty measurement of power readings, the main source of uncertainty for the R was calculated. According to Table 1, it was found in the experimental work which the maximum uncertainty parameter linked with the propagation of uncertainties was around 4.1%, which is a satisfactory value in engineering applications [43].

2.2.5. Validation

The experimental data are equated with the current numerical technique for acting the validation. The model of validation is a heat pipe which is loaded with DW and 0.06 wt% concentrations of nanofluid as working fluid. The heat input to the heaters was set to 100 W and the tilt angle was set 0 degree. However, the heat removed by cooling water at the condenser section was calculated as 92.4 W with a discrepancy of ±14.5%. The result associated with this comparison is shown in Figure 8 as well as the deviation. as claimed by this figure, the highest deviation is lesser than 6%, and therefore the numerical procedure is valid. The source of error can be attributed to the following factors:

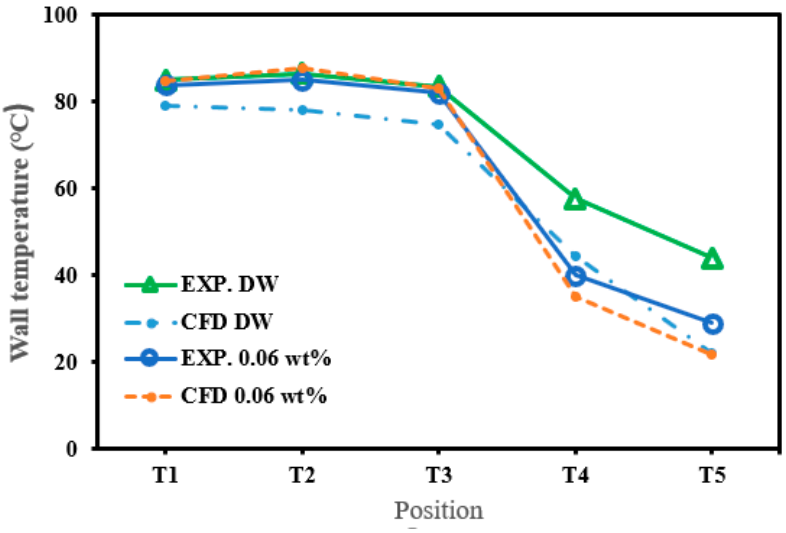

Figure 8. Comparison of numerical to experimental results at 0 degree and 100 W heat input condition.

The temperatures at the condenser section measured by the surface thermocouples might be affected by

- The water flowing in the cooling jacket.
- The non-uniformity in the wick thickness.

3. Results and Discussion

3.1. Thermal Studies

The experimental investigations carry out a preliminary test through sintered heat pipes till achieved the dry out conditions in the evaporator to determine their performance. Figure 9a–d are shown the distributions of temperature at the outer surface of the heat pipe filled with DW as the reference working fluid for various tilt angles (θ = 0°,30°, 60°, 90°). The outer surface temperatures affect the performance and capacity of heat transport for the heat pipe that could be enhanced via a careful choice of working fluid, design of heat pipe, and incline angle. Due to the gravity effect on the working fluid, the temperature of the outer surface is minor at vertical (θ = 90°) position than horizontal (θ = 0°) position, as seen in Figure 9. The differences in temperature amongst the evaporator

and the condenser sections steadily grow with developing the rate of heat input. Furthermore, the steady temperatures of all the wall points show that the heat pipe was activated effectively at this amount of input power. This difference of temperature drops as incline angle modifications from θ = 90° to θ = 30° and then escalations as incline angle drops further to θ = 0°. It shows that the gravity and wick capillary action toughly affect the outer surface temperature distribution.

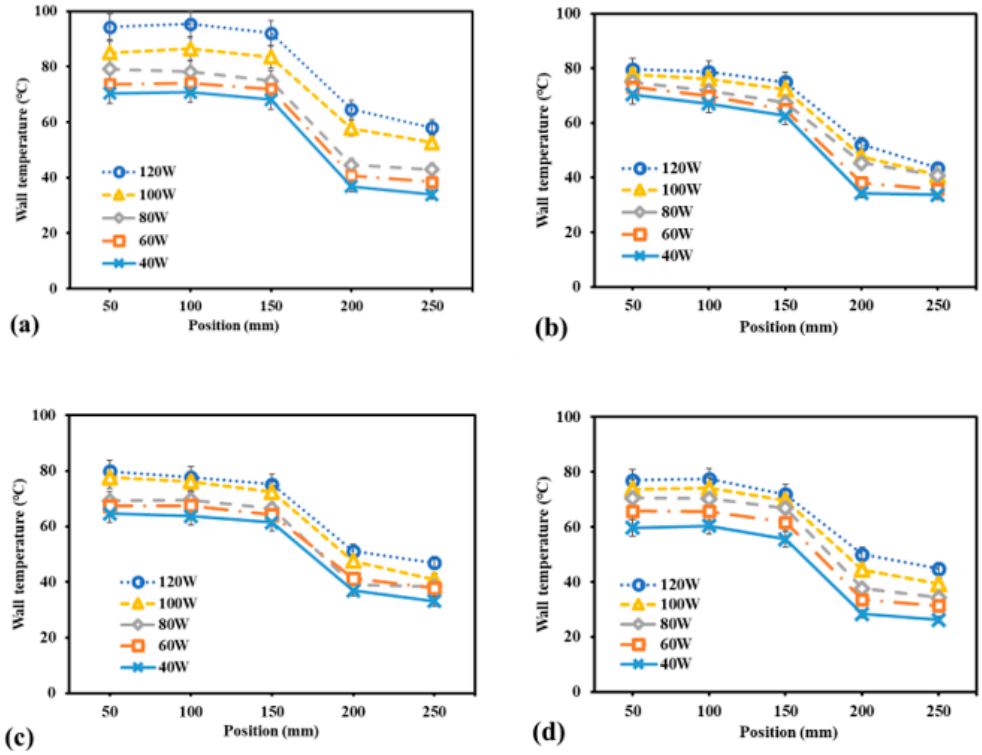

Figure 9. Average of distributions of temperature at the outer surface of the heat pipe that filled by distilled water (DW) for several heat power inputs and inclines angles (θ): (**a**) 0°, (**b**) 30°, (**c**) 60°, (**d**) 90°.

Figure 10 shows a representative result from tests held under dissimilar conditions. The dissimilarity of the temperature amongst evaporator and condenser sections at the outer surface temperature decreases to 30.5 °C with 40 W input power, 0.06 wt% concentration and θ = 90° (Figure 10c) associated to the example of a DW working fluid; the temperature drops to 25 °C (Figure 10a), at same input power. Furthermore, dry out condition could be observed for the heat pipe working with DW with an input power of 120 W (Figure 10b), on the other hand, the heat pipes with PCA-functionalized graphene nanofluids still working at the same input power (Figure 10d). The fact of the dry out condition occurs, when the working fluids block by the bubbles from coming back to the evaporator section during the high heat flux. According to the literature, the boiling limit growths in the heat pipe when using nanofluids as working fluids. Therefore, the dry out phenomenon of the heat pipe could happen at greater inputs.

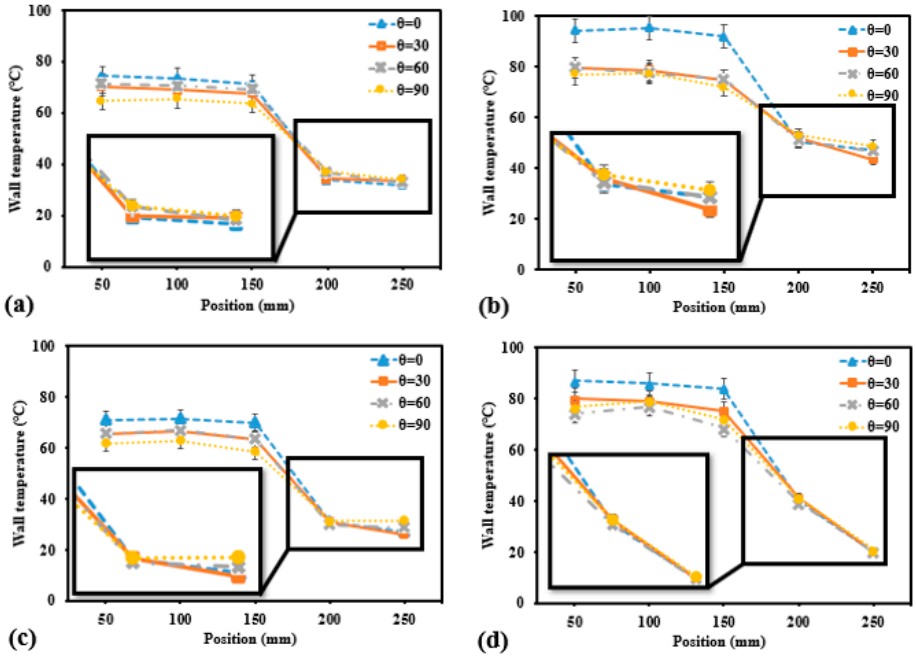

Figure 10. Average of distributions of temperature at the outer surface of heat pipe with a DW and 0.06 wt% PCA-functionalized graphene in different tilt angles, healing inputs; (**a**) DW, 40 W, (**b**) DW, 120 W, (**c**) 0.06 wt% PCA-functionalized graphene, 40 W, (**d**) 0.06 wt% PCA-functionalized graphene, 120 W.

3.2. *Efficiency*

Five heat inputs of 40, 60, 80, 100, and 120 W were applied to estimate the thermal efficiency of the heat pipe filled by PCA-functionalized graphene nanofluids besides DW. Figure 11 demonstrates the consequence of heat input on the thermal efficiency of the heat pipe for several tilt angles and different working fluids. The thermal efficiency rises with heat input since, at greater heat powers, the thermal resistance is minor. In this example, the produced vapor bubbles freely burst through their fabrication as an outcome of contact with nanoparticle surfaces. Similarly, in the liquid–solid interface preparation of bubble layers could be a different reason for the reduction of heat transfer rate, which could be prohibited by using nanoparticles. The direction of the heat pipe has a momentous effect on the efficiency that slowly rises with the tilt angle.

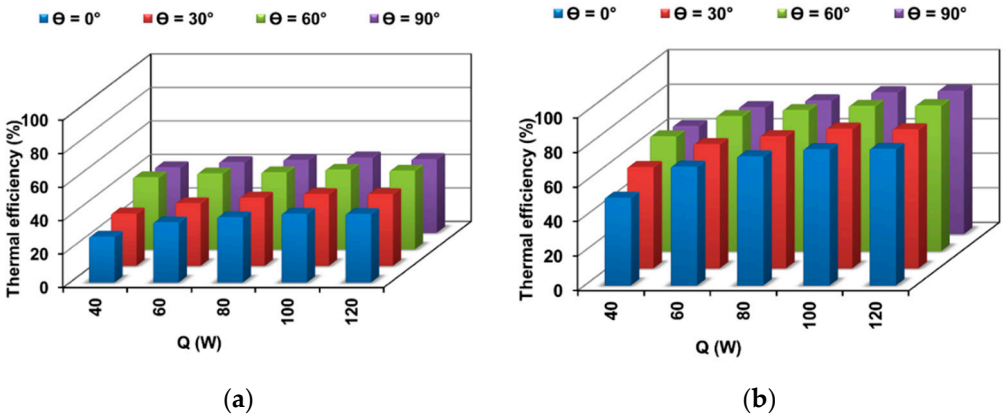

Figure 11. Thermal efficiency analysis associated with different load power and tilt angles and various working fluids; (**a**) DW, (**b**) 0.06 wt% PCA-functionalized graphene.

The results indicate that the highest thermal efficiency of 79% was accomplished for the 0.06 wt% of PCA-functionalized graphene nanofluids at the power of 120 W, demonstrating almost 49% enrichment as compared to the DW at similar operational settings (Figure 11).

3.3. Temperature Distribution of Simulation

The governing Equations (7)–(19) were numerically solved by considering all of boundary and primary conditions. Heat power input sat at 40 W and 120 W. The preliminary pressure and temperature of domain are presumed as 3778 Pascal and 20 °C, separately [41]. The coolant fluid temperature or the free stream (Tc) is implicit as 20 °C. For DW and 0.06 wt% PCA-functionalized graphene in the absence of the deposition of nanoparticles, the effective thermal conductivity of the wick is found to be 1.11 and 1.78 W/m-K, respectively. The effective temperature difference between the heat source to the evaporator and the heat sink from the condenser is proportional to the overall rate of heat transfer in the system [44], and in reverse comparative to the heat transfer of equivalent thermal resistance between the two regions. Figure 12 shows the predicted wall temperatures distribution from the evaporator section to the condenser in different working angles and 40 W power input. The temperature difference between 0.06 wt% PCA-functionalized graphene nanofluid concentrations and DW at the evaporator section are approximately 8 °C for an inclined angle of θ = 0°. However, the temperatures of the outer surface of the heat pipe occupied by PCA-functionalized graphene nanofluid for similar settings and an incline angle of θ = 90° are 4.1 °C lower than while used DW as the working fluid.

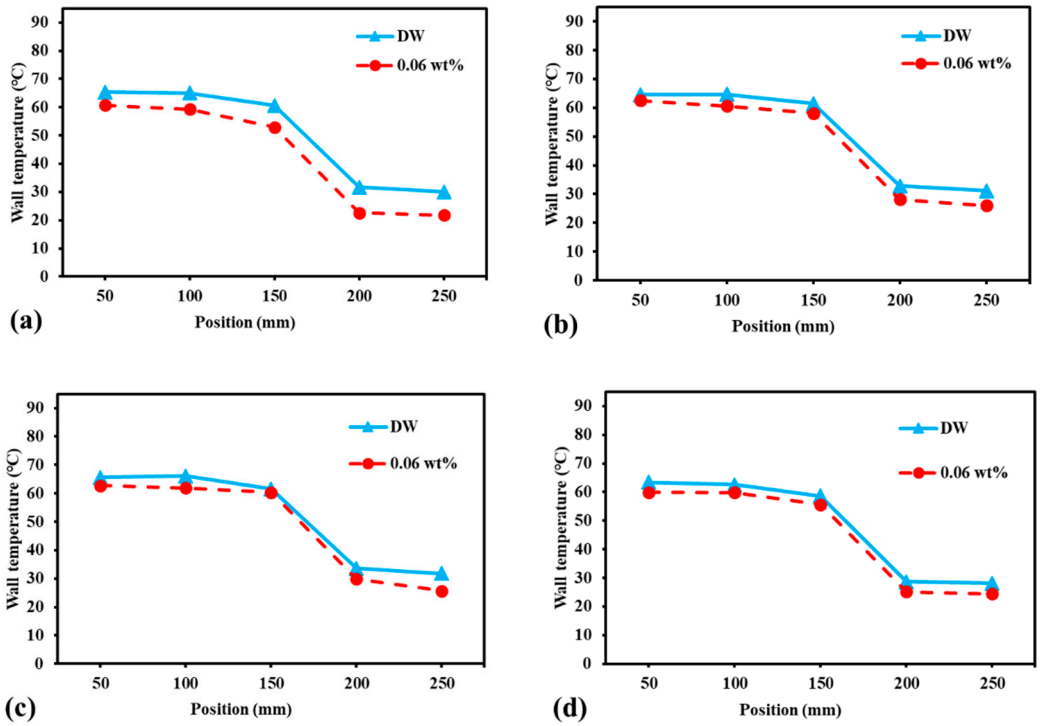

Figure 12. Distribution of surface temperature along heat pipe with a DW and 0.06 wt% PCA-functionalized graphene working fluid for heat input of 40 W and four tilt angles (θ): (**a**) 0°, (**b**) 30°, (**c**) 60°, (**d**) 90°.

3.4. Flow Visualization of CFD Simulation Results

Due to density difference, the vapor's movement from the heating section to the cooling section could happen typically, while the return of the cooling section to the heating section is because of the gravity and force of capillary action in the wick structure. Changing the orientation of the heat pipe from 0° to 90°, remarkably increased the flow of liquid to the evaporator section due to the

gravitational impact. This causes to decrease the heat transfer in the outward direction and growths the thermal resistance of the heat pipe.

Figure 13 shows the effect of gravity on the centerline of the heat pipe that changes the volume fraction of vapor in different heat input. The differences in volume fraction amongst the evaporator and the condenser sections steadily grow with increasing the rate of heat input from 40 W to 120 W. The blue color indicates the minimum volume of vapor in the condenser section that could explain the return of working fluid from the condenser to the evaporator section. Due to gravity, fluid returns through the bottom line of the heat pipe as shown in Figure 13.

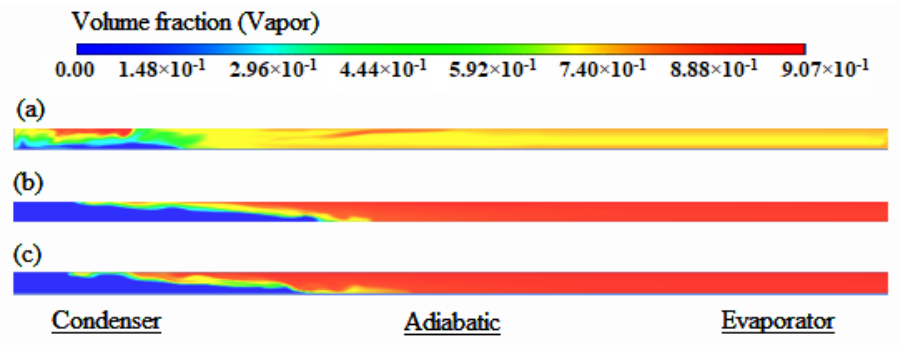

Figure 13. Volume fraction of vapor in 0° title angle effected by heat input (**a**) 40 W, (**b**) 80 W, and (**c**) 120 W.

Similarly, Figure 14 illustrated the velocity magnitude of the mixture at 60 W and 100 W heat input. The velocity is higher at top of the heat pipeline, as the liquid phase flows at the bottom line of the heat pipe and return from the condenser section to the evaporator section. Correspondingly, it is detected that the velocity grows with the increase in the heat input.

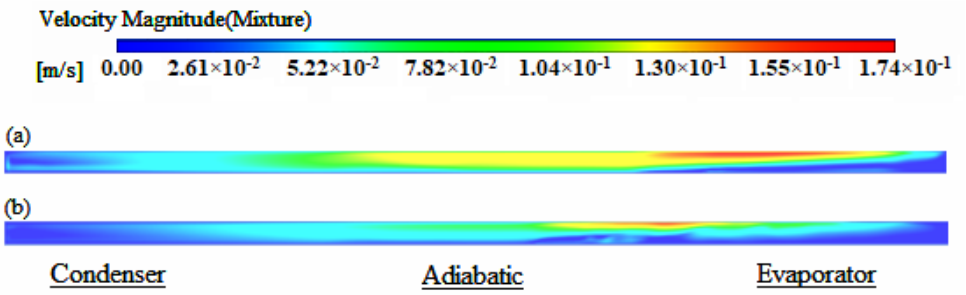

Figure 14. Velocity magnitude in 0° title angle effected by (**a**) 60 W and (**b**) 100 W.

The volume of vapor is slightly more than the volume of water when the temperature and the title angle increase (Figure 15). The liquid phase of working fluid moving from condenser to the adiabatic section due to the gravity force.

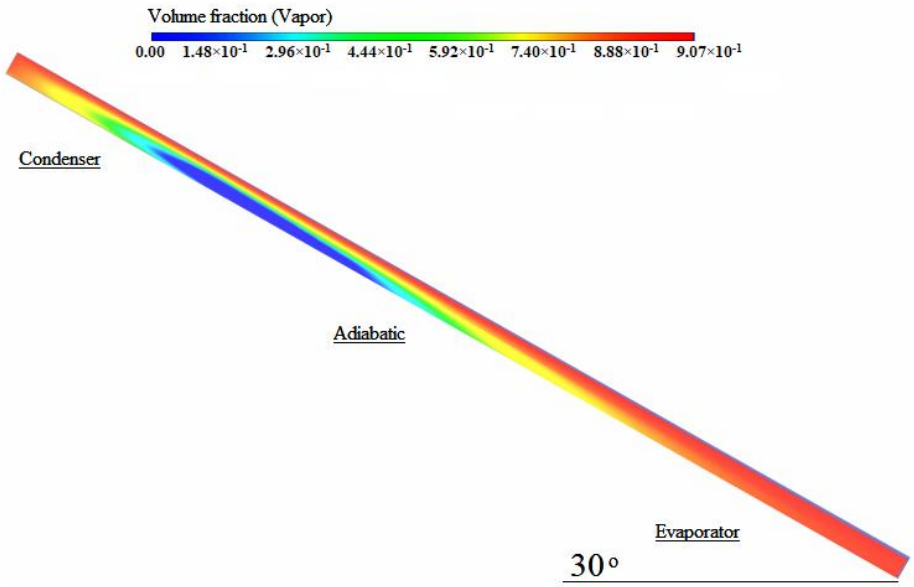

Figure 15. Volume fraction of vapor in 30° title angle effected by 120 W.

Figure 16 indicated the velocity magnitude contours in the vapor chamber for 30 degrees and heated by 100 W, the maximum fluid velocity is 0.174 m/s. It shows that velocity is zero at the start of the evaporator end slowly grows towards the top of the adiabatic section and develops maximum at the beginning of adiabatic and remains sustained along the adiabatic and regularly decreases and becomes zero at the condenser.

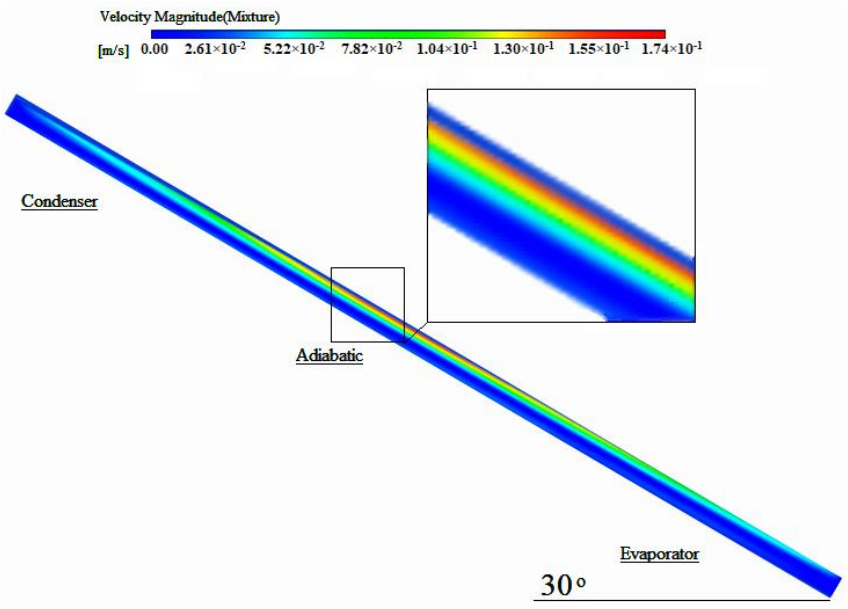

Figure 16. Velocity magnitude in 30° title angle effected by 100 W.

In Figure 17, the volume fraction of vapor in 90° by heat pipe at working input power in the range 40–120 W. According to the volume fraction profile, the liquid phase is more on the condenser section. The gravity provides the maximum help to the liquid phase for simply return to the evaporator section, at this angle. Results indicate that the heat pipe can transfer heat at any working position besides the horizontal position.

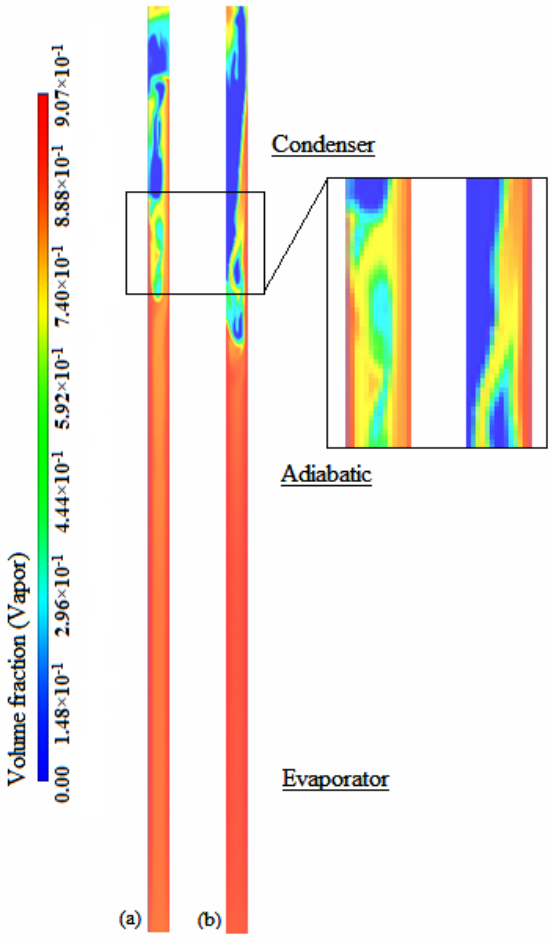

Figure 17. Volume fraction of vapor in 90° title angle effected by heat input (**a**) 40 W and (**b**) 120 W.

4. Conclusions

In this work, a study was prepared to evaluate the application of PCA-functionalized graphene nanofluids at concentrations 0.06 wt% inside sintered wick heat pipe and model's validation of the two-phase VOF numerical model. In addition, investigate the heat pipe thermal performance in the different input power rates and heat pipe tilt angles, which can be suitable for the various thermal applications. The methodical experiments achieved the outer surface temperature and efficiency of the heat pipe. For the inclination angle, larger values of angle amplified the gravity initiating in a massive reduction of the condenser, however providing an exceptional return of the liquid working fluid from the condenser to the evaporator. It is perceived that the liquid and vapor velocity grow with the increase in the heat power input. A tilting angle of $\theta = 90°$ produces the most excellent overall thermal performance in every sample, emphasizing the significance of gravitational forces. The presence of PCA-functionalized graphene nanofluids decreased the thermal resistance and amplified the heat transfer coefficient of the heating section and deliver the occasion for decreasing its size for the same operating conditions.

Author Contributions: Conceptualization: H.S.C.M. and A.E.; methodology: A.E.; validation, A.E., M.S., and S.I.; formal analysis: S.I.; investigation, M.S.N.S.; resources: H.S.C.M.; writing—original draft preparation, A.E.; writing—review and editing, M.S.N.S. and M.S.; visualization, A.B.M.; supervision, H.S.C.M.; project administration, N.N.N.G.; funding acquisition, N.N.N.G. All authors have read and agreed to the published version of the manuscript.

Funding: This work was supported by University of Malaya, Grant number: RP006C-13AET.

Conflicts of Interest: The authors declare no conflict of interest.

References

1. Pawar, V.R.; Sobhansarbandi, S. CFD modeling of a thermal energy storage based heat pipe evacuated tube solar collector. *J. Energy Storage* **2020**, *30*, 101528. [CrossRef]
2. Mofijur, M.; Mahlia, T.M.I.; Silitonga, A.S.; Ong, H.C.; Silakhori, M.; Hasan, M.H.; Putra, N.; Rahman, S.M.A. Phase Change Materials (PCM) for Solar Energy Usages and Storage: An Overview. *Energies* **2019**, *12*, 3167. [CrossRef]
3. Naghavi, M.S.; Ong, K.S.; Badruddin, I.A.; Mehrali, M.; Silakhori, M.; Metselaar, H.S.C. Theoretical model of an evacuated tube heat pipe solar collector integrated with phase change material. *Energy* **2015**, *91*, 911–924. [CrossRef]
4. Sarafraz, M.; Tlili, I.; Tian, Z.; Bakouri, M.; Safaei, M.R. Smart optimization of a thermosyphon heat pipe for an evacuated tube solar collector using response surface methodology (RSM). *Phys. A Stat. Mech. Its Appl.* **2019**, *534*, 122146. [CrossRef]
5. Sundar, L.S.; Sharma, K.; Singh, M.K.; Sousa, A. Hybrid nanofluids preparation, thermal properties, heat transfer and friction factor–A review. *Renew. Sustain. Energy Rev.* **2017**, *68*, 185–198. [CrossRef]
6. Faghri, A. Review and advances in heat pipe science and technology. *J. Heat Transf.* **2012**, *134*, 123001. [CrossRef]
7. Maydanik, Y.; Vershinin, S.; Chernysheva, M. Investigation of thermal characteristics of a loop heat pipe in a wide range of external conditions. *Int. J. Heat Mass Transf.* **2020**, *147*, 118967. [CrossRef]
8. Reay, D.; McGlen, R.; Kew, P. *Heat Pipes: Theory, Design and Applications*; Butterworth-Heinemann: Oxford, UK, 2013.
9. Rostami, S.; Toghraie, D.; Shabani, B.; Sina, N.; Barnoon, P. Measurement of the thermal conductivity of MWCNT-CuO/water hybrid nanofluid using artificial neural networks (ANNs). *J. Therm. Anal. Calorim.* **2020**, 1–9. [CrossRef]
10. Silakhori, M.; Metselaar, H.; Mahlia, T.; Fauzi, H. Preparation and characterisation of microencapsulated paraffin wax with polyaniline-based polymer shells for thermal energy storage. *Mater. Res. Innov.* **2014**, *18* (Suppl. 6), 480–484. [CrossRef]
11. Silakhori, M.; Jafarian, M.; Arjomandi, M.; Nathan, G.J. Comparing the thermodynamic potential of alternative liquid metal oxides for the storage of solar thermal energy. *Sol. Energy* **2017**, *157*, 251–258. [CrossRef]
12. Jouhara, H.; Meskimmon, R. Experimental investigation of wraparound loop heat pipe heat exchanger used in energy efficient air handling units. *Energy* **2010**, *35*, 4592–4599. [CrossRef]
13. Weng, Y.-C.; Cho, H.-P.; Chang, C.-C.; Chen, S.-L. Heat pipe with PCM for electronic cooling. *Appl. Energy* **2011**, *88*, 1825–1833. [CrossRef]
14. Wong, S.-C.; Tseng, H.-H.; Chen, S.-H. Visualization experiments on the condensation process in heat pipe wicks. *Int. J. Heat Mass Transf.* **2014**, *68*, 625–632. [CrossRef]
15. Sureshkumar, R.; Mohideen, S.T.; Nethaji, N. Heat transfer characteristics of nanofluids in heat pipes: A review. *Renew. Sustain. Energy Rev.* **2013**, *20*, 397–410. [CrossRef]
16. Cacua, K.; Buitrago-Sierra, R.; Herrera, B.; Pabón, E.; Murshed, S.S. Nanofluids' stability effects on the thermal performance of heat pipes. *J. Therm. Anal. Calorim.* **2019**, *136*, 1597–1614. [CrossRef]
17. Gupta, N.K.; Tiwari, A.K.; Ghosh, S.K. Heat transfer mechanisms in heat pipes using nanofluids—A review. *Exp. Therm. Fluid Sci.* **2018**, *90*, 84–100. [CrossRef]
18. Li, Z.; Sarafraz, M.; Mazinani, A.; Moria, H.; Tlili, I.; Alkanhal, T.A.; Goodarzi, M.; Safaei, M.R. Operation analysis, response and performance evaluation of a pulsating heat pipe for low temperature heat recovery. *Energy Convers. Manag.* **2020**, *222*, 113230. [CrossRef]
19. Goshayeshi, H.R.; Goodarzi, M.; Safaei, M.R.; Dahari, M. Experimental study on the effect of inclination angle on heat transfer enhancement of a ferrofluid in a closed loop oscillating heat pipe under magnetic field. *Exp. Therm. Fluid Sci.* **2016**, *74*, 265–270. [CrossRef]
20. Kim, K.M.; Jeong, Y.S.; Kim, I.G.; Bang, I.C. Comparison of thermal performances of water-filled, SiC nanofluid-filled and SiC nanoparticles-coated heat pipes. *Int. J. Heat Mass Transf.* **2015**, *88*, 862–871. [CrossRef]
21. Mehrali, M.; Sadeghinezhad, E.; Latibari, S.T.; Kazi, S.N.; Mehrali, M.; Zubir, M.N.B.M.; Metselaar, H.S.C. Investigation of thermal conductivity and rheological properties of nanofluids containing graphene nanoplatelets. *Nanoscale Res. Lett.* **2014**, *9*, 15. [CrossRef]

22. Goodarzi, M.; Rashidi, M.M.; Basiriparsa, A. Analytical and numerical solutions of vapor flow in a flat plate heat pipe. *Walailak J. Sci. Technol. (WJST)* **2012**, *9*, 65–81.
23. Ghanbarpour, M.; Nikkam, N.; Khodabandeh, R.; Toprak, M.S.; Muhammed, M. Thermal performance of screen mesh heat pipe with Al_2O_3 nanofluid. *Exp. Therm. Fluid Sci.* **2015**, *66*, 213–220. [CrossRef]
24. Naphon, P.; Assadamongkol, P.; Borirak, T. Experimental investigation of titanium nanofluids on the heat pipe thermal efficiency. *Int. Commun. In Heat Mass Transf.* **2008**, *35*, 1316–1319. [CrossRef]
25. Goshayeshi, H.R.; Safaei, M.R.; Goodarzi, M.; Dahari, M. Particle size and type effects on heat transfer enhancement of Ferro-nanofluids in a pulsating heat pipe. *Powder Technol.* **2016**, *301*, 1218–1226. [CrossRef]
26. Iranmanesh, S.; Mehrali, M.; Sadeghinezhad, E.; Ang, B.C.; Ong, H.C.; Esmaeilzadeh, A. Evaluation of viscosity and thermal conductivity of graphene nanoplatelets nanofluids through a combined experimental–statistical approach using respond surface methodology method. *Int. Commun. Heat Mass Transf.* **2016**, *79*, 74–80. [CrossRef]
27. Legierski, J.; Wie, B.; De Mey, G. Measurements and simulations of transient characteristics of heat pipes. *Microelectron. Reliab.* **2006**, *46*, 109–115. [CrossRef]
28. Zhang, M.; Lai, Y.; Zhang, J.; Sun, Z. Numerical study on cooling characteristics of two-phase closed thermosyphon embankment in permafrost regions. *Cold Reg. Sci. Technol.* **2011**, *65*, 203–210. [CrossRef]
29. Joudi, K.A.; Al-Tabbakh, A.A. Computer simulation of a two phase thermosyphon solar domestic hot water heating system. *Energy Convers. Manag.* **1999**, *40*, 775–793. [CrossRef]
30. Annamalai, S.A.; Ramalingam, V. Experimental investigation and CFD analysis of a air cooled condenser heat pipe. *Therm. Sci.* **2011**, *15*, 759–772. [CrossRef]
31. De Schepper, S.C.; Heynderickx, G.J.; Marin, G.B. Modeling the evaporation of a hydrocarbon feedstock in the convection section of a steam cracker. *Comput. Chem. Eng.* **2009**, *33*, 122–132. [CrossRef]
32. Zhang, N. Innovative heat pipe systems using a new working fluid. *Int. Commun. In Heat Mass Transf.* **2001**, *28*, 1025–1033. [CrossRef]
33. Sarafraz, M.M.; Tlili, I.; Tian, Z.; Bakouri, M.; Safaei, M.R.; Goodarzi, M. Thermal evaluation of graphene nanoplatelets nanofluid in a fast-responding HP with the potential use in solar systems in smart cities. *Appl. Sci.* **2019**, *9*, 2101. [CrossRef]
34. Li, L.L.; Liu, K.P.; Yang, G.H.; Wang, C.M.; Zhang, J.R.; Zhu, J.J. Fabrication of graphene—Quantum dots composites for sensitive electrogenerated chemiluminescence immunosensing. *Adv. Funct. Mater.* **2011**, *21*, 869–878. [CrossRef]
35. Soleymaniha, M.; Amiri, A.; Shanbedi, M.; Chew, B.T.; Wongwises, S. Water-based graphene quantum dots dispersion as a high-performance long-term stable nanofluid for two-phased closed thermosyphons. *Int. Commun. Heat Mass Transf.* **2018**, *95*, 147–154. [CrossRef]
36. Ghosh, S.; An, X.; Shah, R.; Rawat, D.; Dave, B.; Kar, S.; Talapatra, S. Effect of 1-pyrene carboxylic-acid functionalization of graphene on its capacitive energy storage. *J. Phys. Chem. C* **2012**, *116*, 20688–20693. [CrossRef]
37. Simmons, T.J.; Bult, J.; Hashim, D.P.; Linhardt, R.J.; Ajayan, P.M. Noncovalent functionalization as an alternative to oxidative acid treatment of single wall carbon nanotubes with applications for polymer composites. *Acs Nano* **2009**, *3*, 865–870. [CrossRef]
38. Churchill, S.; Bernstein, M. A correlating equation for forced convection from gases and liquids to a circular cylinder in crossflow. *J. Heat Transf.* **1977**, *99*, 300–306. [CrossRef]
39. Nemec, P. Gravity in heat pipe Technology. In *Gravity-Geoscience Applications, Industrial Technology and Quantum Aspect*; InTech: Rijeka, Croatia, 2017; p. 7.
40. Fadhl, B.; Wrobel, L.C.; Jouhara, H. CFD modelling of a two-phase closed thermosyphon charged with R134a and R404a. *Appl. Therm. Eng.* **2015**, *78*, 482–490. [CrossRef]
41. Solomon, A.B.; Ramachandran, K.; Asirvatham, L.G.; Pillai, B. Numerical analysis of a screen mesh wick heat pipe with Cu/water nanofluid. *Int. J. Heat Mass Transf.* **2014**, *75*, 523–533. [CrossRef]
42. FLUENT, ANSYS. *User Guide (Release 13.0). Modelling Multiphase Flows*; ANSYS Inc.: Canonsburg, PA, USA, 2010; pp. e1143–e1144.
43. Taylor, J. *Introduction to Error Analysis, the Study of Uncertainties in Physical Measurements*; University Science Books: New York, NY, USA, 1997.

44. Fadhl, B.; Wrobel, L.C.; Jouhara, H. Numerical modelling of the temperature distribution in a two-phase closed thermosyphon. *Appl. Therm. Eng.* **2013**, *60*, 122–131. [CrossRef]